



Host-guest-induced electronic state triggers two-electron oxygen reduction electrocatalysis

Received: 9 May 2024

Accepted: 21 October 2024

Published online: 25 October 2024

 Check for updatesHongni Chen, Chao Wang, Han Wu, Lili Li, Yali Xing, Chuanhui Zhang & Xiaojing Long  

Supramolecular polymers possess great potential in catalysis owing to their distinctive molecular recognition and dynamic crosslinking features. However, investigating supramolecular electrocatalysts with high efficiency in oxygen reduction reaction to hydrogen peroxide (ORHP) remains an unexplored frontier. Herein, we present organic polymers for ORHP by introducing cyclodextrin-containing noncovalent building blocks, affording these supramolecules with abundant dynamic bonds. The electronic states and reaction kinetics are further well-modulated via a host-guest strategy, resulting in appropriate regional electron binding force and controllable chemical activity. Notably, integrating supramolecular units into phenyl group-containing model covalent polymer achieves a production rate of $9.14 \text{ mol g}^{-1} \text{ cat h}^{-1}$, with 98.01% Faraday efficiency, surpassing most reported metal-free electrocatalysts. Moreover, the dynamic bonds in supramolecular catalysts can effectively regulate the binding ability of oxygen intermediates, leading to high reactivity and selectivity for the $2e^-$ pathway. Supported by theory calculation and in situ experiment, C atoms (site-1) adjacent to the $-C=N$ (N) group are potential active sites. This work pioneers host-guest strategy and provides inspiring ideas for the ORHP process.

Hydrogen peroxide (H_2O_2) is a high-value chemical extensively used in energy storage, sewage treatments, healthcare disinfection, and pulp bleaching^{1–3}. Currently, the waste-intensive anthraquinone oxidation process, which causes environmental issues and severe safety for industrial manufacture of H_2O_2 , requires expensive catalysts and causes considerable energy consumption^{4,5}. Due to the gentle aqueous circumstance and ability to supply sustainable and green electricity, electrochemical $2e^-$ oxygen reduction reaction (ORR) represents a promising route for clean and green H_2O_2 production^{6,7}. The key to promoting the target in this booming field is efficiently designing great electroactive catalysts with high selectivity and intensively exploring the catalytic mechanisms for the ORHP process^{8–10}. Metal-free carbon-based materials have been perceived as the most prospective alternatives to commercialized precious metal-based electrocatalysts^{11,12}.

Although most of these reported carbon-based catalysts have demonstrated high catalytic performance for H_2O_2 synthesis, they face enormous challenges in achieving high product concentration and production rate^{13,14}. Thus, it is imperative to design metal-free carbon catalysts with directional $2e^-$ -selectivity and great ORR activity for H_2O_2 electrosynthesis.

Supramolecular chemistry represents the exciting field of chemistry focusing on molecular self-assembly and recognition of diversified constitutional units through non-covalent weak interactions, including hydrophobic interactions, hydrogen bond interactions, π - π interactions, and host-guest interactions^{15–17}. Among these non-covalent interactions, host-guest interactions with macrocyclic components, for instance, rotaxanes, macrocyclic hydrocarbons, cucurbit[8]uril, and cyclodextrins, in supramolecular systems, show

fascinating applications in bioscience and materials science^{18,19}. In particular, macromolecular group/linear polymer-based host-guest catalysts show precise and high catalytic activity because of the supramolecular active coordination bonds and the free delocalized π -electron^{20,21}. In addition, the dynamic regulation of reactivity also plays a crucial role, based on constructing metal-free organic polymers with well-defined periodic structures, the introduction of supramolecular encapsulation enables precise and reversible control over the reaction rate through in situ adjustment of catalyst availability, thereby achieving higher catalytic activity.

In contrast to the traditional design strategy of metal-free carbon-based electrocatalysts, we introduced beta-cyclodextrin (β -CD)-adamantane noncovalent building blocks to develop supramolecular three-dimensional network polymer using a dynamic non-covalent strategy. β -CD, a traditional class of host cyclophane, is a non-toxic, relatively water-soluble conical compound with a particular hydrophobic cavity and hydrophilic rim, which makes it possible to act on the microenvironment of catalytic active sites, as a result of impacting the mass transport and distribution of oxygen intermediate species and affecting the reaction kinetics^{22,23}. In addition, the β -CD-containing host-guest structures can also regulate the electron localization of these organic molecular skeletons, facilitating the charge redistribution in the active region^{24,25}. More importantly, organic skeletons based on host-guest dynamic crosslinking can also effectively manipulate electronic states compared to traditional covalent bonds, exhibiting relatively high conductivity, density activity, and moderate oxygen adsorption, which are conducive to minimizing the thermodynamic barrier of $2e^-$ ORR, thereby facilitating the OOH^* protonation and subsequent H_2O_2 desorption^{26,27}. Thus, maintaining the molecular framework accurately fixed while simultaneously optimizing the electronic structure and regulating the electrocatalytic dynamics through host-guest chemical strategy offers an ideal platform to investigate the interplay between molecular structure and catalytic activity.

In this study, we have developed two dynamic crosslinked supramolecular electrocatalysts (HG-CD-Ph and HG-CD-TPB) by inserting host-guest building blocks into conjugated microporous molecular skeleton models P-CN-Ph and P-CN-TPB with pure carbon linker and triangular knots (Fig. 1). The β -CD-adamantane noncovalent inclusive structure was cleverly introduced to regulate the electron states of carbon-based organic electrocatalysts according to the concept of bee pollination. Both two host-guest-based supramolecular polymers exhibit good production rate and selectivity compared to those analogous models P-CN-Ph and P-CN-TPB, precisely proving that the host-guest dynamic bonds endow C atoms of adamantane (site-1) adjacent to $-C=N$ (N) group as valid active sites for ORHP. Most remarkably, due to the superiority of typical donor-acceptor (D-A) properties and moderate absorption of oxygen intermediates in the $2e^-$ ORR process, the central phenyl group-containing HG-CD-Ph with dynamic bond achieves a high production rate ($9.14 \text{ mol g}^{-1} \text{ cat h}^{-1}$) and Faraday efficiency (98.01%), surpassing most reported metal-free electrocatalysts. Diverse in situ experimental and theoretical data demonstrate that the unique dynamic structural decoration facilitates adjustable charge localization, appropriate bandgap for efficient charge transfer, and optimized free energy of oxygen intermediates during the ORHP process.

Results

Synthesis of covalent-linked polymers and dynamic-crosslinked supramolecular polymers

To implement the dynamic and covalent bond strategy and intuitively investigate the influence of various bonding modes on catalytic activity, 4,4'-Biphenyldiamine (BD), serving as a linear linker, 1,3,5-Tris-(p-formylphenyl) benzene (TPB) and 1,3,5-Benzenetricarboxaldehyde (Ph) as planar building units were utilized to directly synthesize two conjugated microporous polymers under optimized solvothermal

conditions, denoted as P-CN-TPB and P-CN-Ph. Two supramolecular polymers, HG-CD-TPB and HG-CD-Ph, were further generated through the introduction of β -CD-adamantine noncovalent building blocks. Figure 1 illustrates the use of bee pollination to promote flowering maturity by introducing host-guest inclusion structures into conjugated microporous frameworks. The hydrophobic cavity and hydrophilic rim features of β -CD enable the ability to promote the formation of a local electric field in the internal environment and accelerate the transfer of electrons. At the same time, the external hydrophilicity can also improve the electron transport rate. In addition, compared to covalent-linked polymers with analogous skeletons, the host-guest chemistry will endow supramolecular catalysts with dynamic cross-linking structures, enabling self-assembly and self-healing for efficient ORR activity.

The influence of different bonding modes on the electronic environment of metal-free organic molecules was further studied by density functional theory (DFT) calculation (details about molecular configurations can be found in the Supplementary Data 1). The molecular orbital energy level, as a nonnegligible factor for electron distribution, has been extensively studied in electrocatalysis²⁸. As schematically presented in Fig. 2, the host-guest-based HG-CD-TPB and HG-CD-Ph exhibit prominent D-A properties, contributing to charge transfer during the reaction. Quantitative molecular surface analysis was performed by combining electrostatic potential (ESP) and average local ionization energy (ALIE)^{29,30}. In covalently bonded polymers, P-CN-TPB and P-CN-Ph, negative charges are concentrated on the electronegative N atoms, while after the introduction of β -CD-adamantine, most of the charges of HG-CD-TPB and HG-CD-Ph are attracted by the interaction between host and guest forces, breaking the relatively uniform charge distribution within the molecules, which is conducive to the improvement of catalytic activity^{31,32}. Additionally, the minimum ALIE values of both supramolecules and polymers are located proximal to the $-C=N$ (N), indicating a weaker charge binding force, a more vigorous electron activity, and a more accessible occurrence of electrophilic reaction in this region, thereby favoring $2e^-$ ORR^{33,34}.

To analyze the chemical structures of the as-prepared polymers, Fourier transform infrared (FT-IR) spectroscopy was conducted (Fig. 3a). The control polymers P-CN-Ph and P-CN-TPB with covalent bonds exhibited the characteristic $C=N$ stretching vibration mode at 1625 cm^{-1} , accompanied by the absence of the $N-H$ stretching bands of the diamine monomer at 3323 and 3393 cm^{-1} as well as the disappearance of $C=O$ stretching bands of TPB and Ph at 1690 cm^{-1} (Figs. S1–S2). The FT-IR data provides evidence of successful imine condensation between aldehyde and amino monomers³⁵, which is further corroborated by the ^{13}C CP-MAS NMR spectra (Figs. S3–4). In addition, in the ^{13}C CP-MAS NMR spectra, the chemical shifts of β -CD carbon atoms (site-2 and site-3) and adamantane carbon atoms (site-8 and site-9) in HG-CD-TPB and HG-CD-Ph demonstrate notable alterations compared to their precursors (Figs. S5–6), indicating the presence of host-guest interactions within the supramolecular assemblies. The conductivity was further assessed through current-voltage (I-V) tests (Fig. 3b). As can be seen, dynamic-crosslinked supramolecular polymers exhibited higher conductivities compared to covalent-linked microporous polymers. The electronic structure of these electrocatalysts was evaluated using solid ultraviolet-visible diffuse reflectance spectroscopy (UV-vis DRS) (Fig. 3c). In comparison to the covalently bonded P-CN-Ph and P-CN-TPB, the host-guest-based HG-CD-Ph and HG-CD-TPB with smaller band gaps of 1.67 and 2.00 eV, respectively, displayed distinct red-shifted absorption (Fig. S7). Moreover, thermal gravimetric analysis (TGA) and derivative thermogravimetric (DTG) analysis demonstrate the good thermal stability of both synthesized host-guest and covalent bond catalysts (Fig. 3d). The specific surface area and permanent porosity of these catalysts were determined under N_2 adsorption at 77 K (Fig. S8). Notably, the similar surface area values and pore size distribution curves observed for

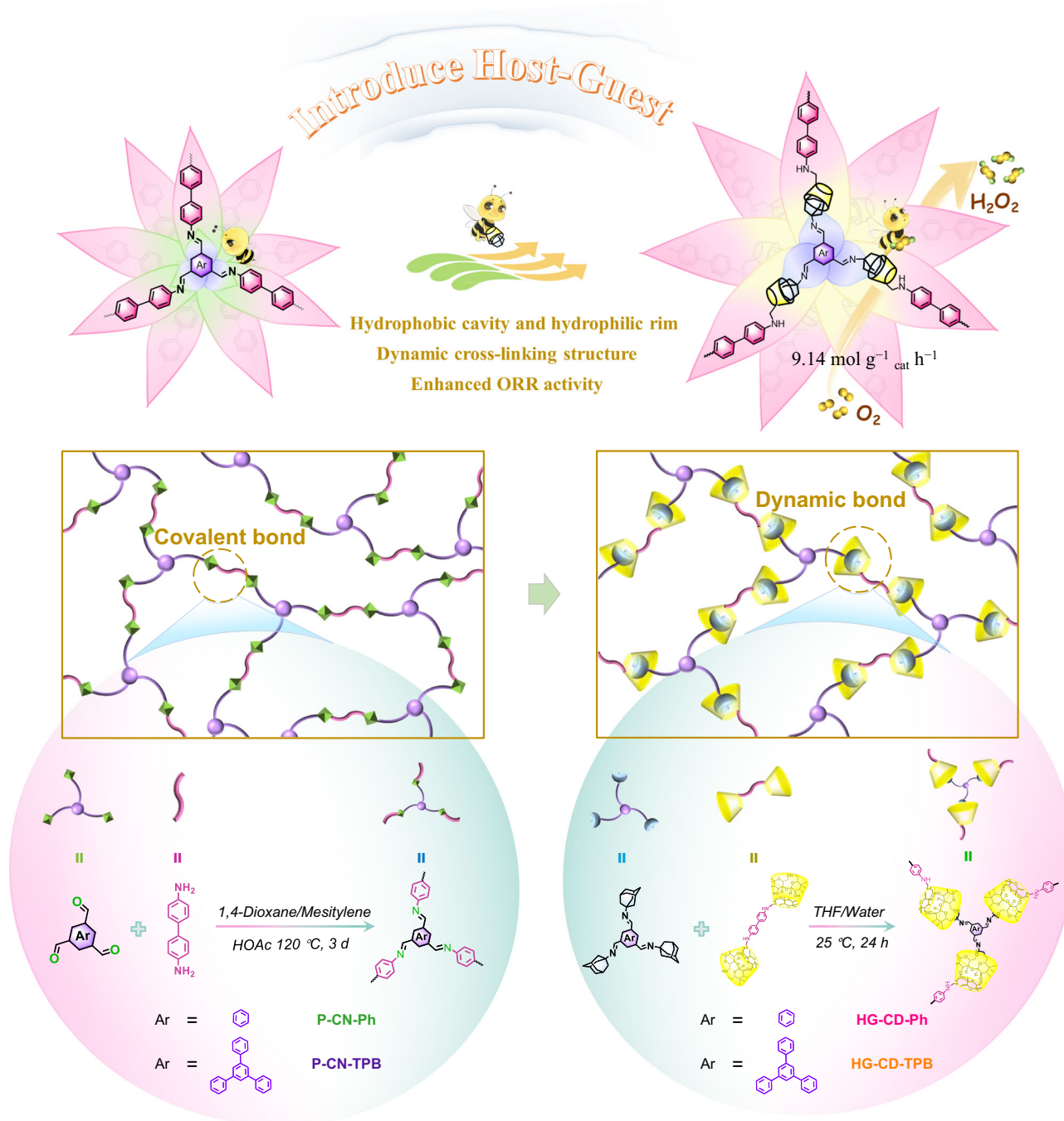


Fig. 1 | Formation of the catalysts. The Illustration of covalent-bonded P-CN-TPB and P-CN-Ph and dynamic-bonded HG-CD-TPB and HG-CD-Ph with host-guest interaction.

these supramolecular and polymer catalysts suggested that the introduction of dynamic bonds did not significantly alter the microscopic porosity and surface area of the covalently bonded polymers (Figs. S9–12). The ORR is widely acknowledged as a three-phase interface reaction involving gas, liquid, and solid phases³⁶. The presence of β -CD within the polymer framework may induce alterations in its wettability. To verify this, the wettability of these electrocatalysts was evaluated through water vapor uptake experiments (Figure S13), wherein the water adsorption capacity of dynamically crosslinked HG-CD-TPB and HG-CD-Ph significantly exceeded those of the model covalent polymers, indicating that the β -CD units serve as the primary drivers for the enhanced hydrophilicity observed in the supramolecular system. The aforementioned results were also validated through

water contact angle measurements (Fig. 3e). Notably, the hydrophilicity of dynamically crosslinked HG-CD-TPB and HG-CD-Ph facilitates the diffusion of oxygen-active species to the catalyst surface. In particular, while maintaining its hydrophilic nature, HG-CD-Ph exhibits a slightly larger contact angle, which favors the formation of a water film. This further strengthens the efficiency of oxygen transport and positively influences the stability of the electrode³⁷.

The amorphous morphology of dynamic-crosslinked supramolecular polymers and covalent-linked polymers was confirmed through Powder X-ray diffraction (PXRD) measurements (Fig. S14). Compared with the PXRD of supramolecular precursors, the disappearance of small molecular peaks in dynamic-crosslinked supramolecular polymers provides preliminary evidence for the formation

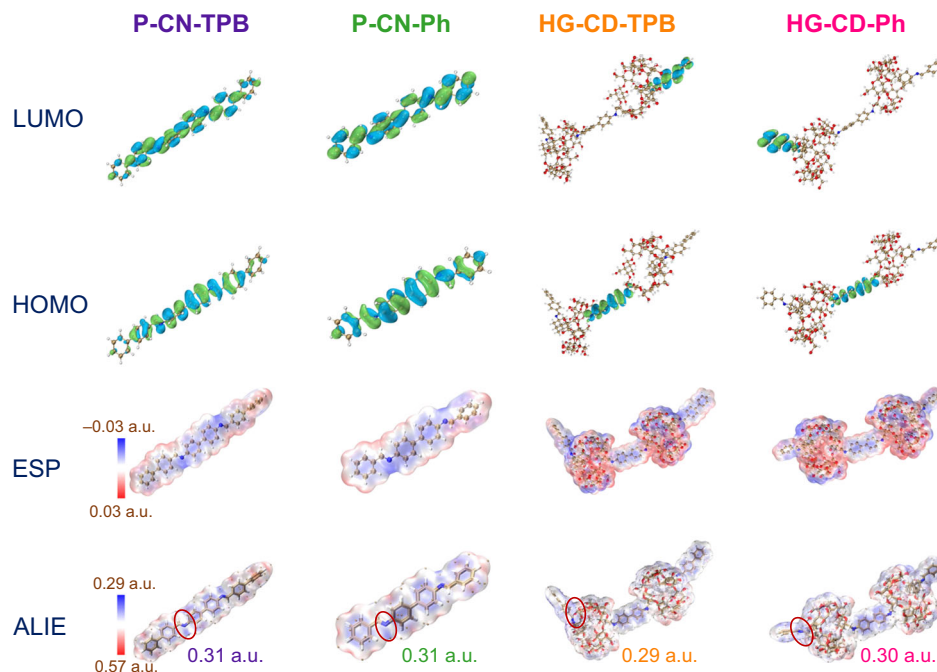


Fig. 2 | Electronic configuration and charge distribution of the catalysts. The Kohn–Sham LUMOs, HOMOs, electrostatic potential surface maps, and the smallest areas of average local ionization energy of P-CN-TPB, P-CN-Ph, HG-CD-TPB, and HG-CD-Ph. Blue, brown, red, and white spheres represent the N, C, O, and H atoms, respectively.

of inclusion complexes between adamantane and β -CD, as well as indicating a host-guest interaction (Figs. S15–16). The FT-IR shift of O–H bonds can further prove that the host-guest interaction is successfully generated (Figs. S17–18)³⁸. Two-dimensional nuclear Overhauser effect spectroscopy (2D NOESY) NMR is an efficient and sensitive method for analyzing near proton interaction. Therefore, it was further employed to precisely confirm the host-guest interaction between adamantane and β -CD. Figure 3f and S19 display the correlation between the $-\text{CH}_2$ protons of adamantanes and the protons (C(3)H and C(5)H) in the β -CD cavity, represented by a green rectangular signal, validating successful self-assembly of the host β -CD and the guest adamantanes^{39,40}. X-ray photoelectron spectroscopy (XPS) was also used to evaluate the electron states of covalently bonded polymers and the dynamic crosslinked supermolecules (Figs. S20–21). As expected, the C–O and C=N–C peaks of HG-CD-TPB and HG-CD-Ph in *C 1s* spectra shift toward higher binding energy compared with cyclodextrin and adamantane monomers (Fig. S22), indicating a significant impact of cyclodextrin on the electronic structure of C=N–C site. The synthesis of host-guest small molecule inclusion complexes provides further validation of the distinct influence that β -CD exerts on the electronic state of the C atoms located adjacent to the C=N (N) group in the adamantane moiety (Fig. S23). In addition, the chemical stability of covalently bonded polymers and the dynamic crosslinked supermolecules was evaluated by immersing them in water for three days or exposing them to an electrochemical ORR test in 0.1M KOH electrolyte. Remarkably, an in-depth analysis of the FT-IR spectra and PXRD patterns revealed the robust stability of these materials under both conditions (Figs. S24–26). Inductively Coupled Plasma Mass Spectrometry (ICP-MS) of electrolytes before and after the stability test was performed to exclude the possible interference of metal contaminants from the device. The results demonstrate that good performance is due to the designed catalysts rather than metal influence (Fig. S27).

Scanning electron microscopy (SEM) showed stacked spheres of covalent-linked polymers and porous masses of dynamic-crosslinked supramolecular polymers (Fig. 4a–d). Specific observations demonstrated that P-CN-TPB exhibits a wire globule-covered sphere, and

P-CN-Ph features a globule-filled sphere, whereas a microporous multi-layer shell of HG-CD-TPB and HG-CD-Ph presents a large porous random cube (Fig. 4e–h), indicating that modifications in the connected bonds resulting from host-guest strategy can significantly affect their growth modes. To gain further insights into the morphology of covalent-linked polymers and dynamic-crosslinked supramolecular polymers, energy-dispersive X-ray spectroscopy (EDS) mapping photos and transmission electron microscopy (TEM) were conducted, confirming the uniform distribution of characteristic elements throughout these materials (Fig. 4i–l).

Electrocatalytic 2e^- -ORR characterizations

To investigate the ORHP properties of these supramolecular catalysts, a rotating ring-disc electrode (RRDE) was used to perform electrochemical tests in an O_2 -saturated 0.1M KOH electrolyte (Fig. S28). Dynamic cross-linking HG-CD-Ph and HG-CD-TPB exhibit higher ring current and activity in ORHP compared to the covalently bonded P-CN-Ph and P-CN-TPB, surpassing the most recently reported catalysts with covalent bond (Fig. 5a–c, 4h and S29–31, and Table S1). Notably, HG-CD-Ph exhibits optimal selectivity for H_2O_2 at 94.93% when operated at 0.4 V vs. RHE. The electron-transfer number of HG-CD-Ph also decreases to 2.10 at 0.4 V, showing an apparent two-electron transfer process. A similar phenomenon is also found in neutral electrolytes (Fig. S32).

Moreover, electrochemical tests conducted on supramolecular precursors (Figs. S33–34) and physical blends with cyclodextrin monomers (Figs. S35–36) revealed significantly diminished performance compared to those of supramolecules HG-CD-TPB and HG-CD-Ph, indicating that the dynamic bond formed through host-guest interaction can effectively regulate the reaction process and enhance the catalytic efficiency. To further elucidate the influence of secondary amines in dynamic crosslinking catalysts on catalytic activity, covalently bonded model polymers containing secondary amines were also synthesized (Figs. S37–38). Theoretical and experimental evidence suggests that the introduction of secondary amines is not pivotal to improving the performance of supramolecular catalysts (Figs. S39–42 and Table S6).

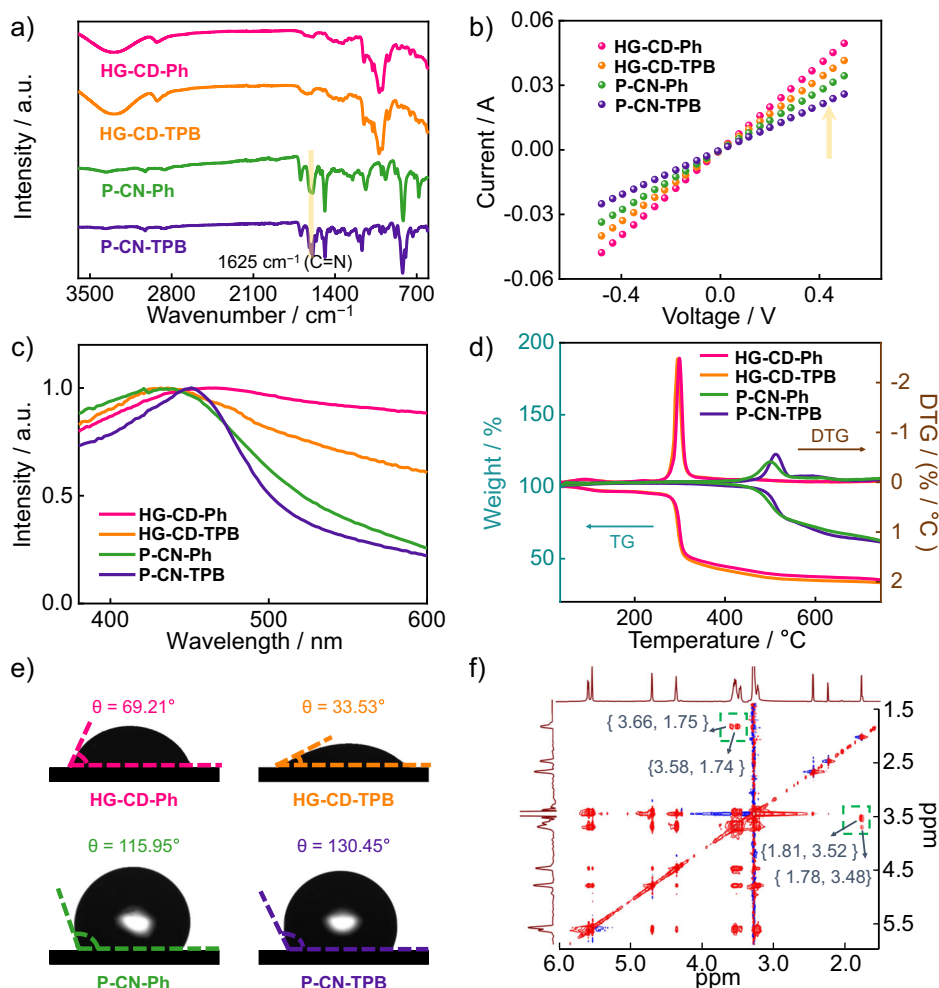


Fig. 3 | Microstructural characterizations of the catalysts. a FT-IR spectra. **b** Room temperature current (*I*)–voltage (*V*) curves. **c** UV-vis diffuse reflectance spectrum. **d** TGA, and DTG curves under N_2 . **e** The contact angles of HG-CD-Ph, HG-CD-TPB, P-CN-Ph, and P-CN-TPB. **f** 2D NOESY spectra (600 MHz, $DMSO-d_6$, 298 K) of HG-CD-Ph.

The disparity in performance between dynamic-crosslinked supramolecules and covalent-linked polymers is ascribed to the distinctly connected bonds, implying that dynamic dual-channel regulation induced by host-guest strategy plays a pivotal role in enhancing electrocatalytic activities^{41,42}. Compared with model P-CN-Ph (77.29 $mV\ dec^{-1}$) and P-CN-TPB (79.81 $mV\ dec^{-1}$), the supramolecular HG-CD-Ph and HG-CD-TPB have smaller Tafel slopes of 75.56 and 76.33 $mV\ dec^{-1}$, respectively, demonstrating the faster charge-transfer kinetics of dynamic-crosslinked supramolecular polymers under alkaline conditions (Fig. 5d). The electrochemically active surface areas (ECSAs) were estimated using the electrochemical double-layer capacitance (C_{dl}) (Fig. 5e and S43–47). The results confirmed that the central phenyl group-containing HG-CD-Ph exhibited the highest C_{dl} value, indicating its superior active density. Furthermore, the smaller curve radius of dynamic-crosslinked supramolecular polymers, as measured by electrochemical impedance spectroscopy (EIS), demonstrated that the host-guest induced D–A structure was conducive to a reduced charge transfer resistance (R_{ct}) (Fig. 5f)⁴³. In addition, the long-term stability of HG-CD-Ph was assessed through a 10-hour test in an O_2 -saturated 0.1 M KOH electrolyte (Fig. 5g). The result shows that HG-CD-Ph maintains great stability for prolonged H_2O_2 production, with a remarkable activity retention rate of 94% for 10 hours at 0.4 V under alkaline conditions.

Motivated by the great $2e^-$ ORR performance observed in RRDE, the H_2O_2 electrosynthesis was investigated on a practical three-phase

flow cell using chronopotentiometry (Fig. 6a). After 1 hour of electrolysis, the H_2O_2 concentration in the electrolyte of cathodic tank was analyzed to calculate the H_2O_2 production rate and Faradic efficiency (FE). To determine the H_2O_2 concentration, traditional $Ce(SO_4)_2$ titration and a well-fitted calibration curve for UV-vis spectrophotometric determination of Ce^{4+} in an aqueous solution were performed (Figs. S48–49). The yield and FE at different constant currents revealed that HG-CD-Ph exhibited the highest FE value at 80 $mA\ cm^{-2}$ (Fig. 6b and S50). The yields of other samples at 80 $mA\ cm^{-2}$ were selected for comparison (Figs. S51–54). The H_2O_2 yield of HG-CD-Ph is remarkably high at 9.14 $mol\ g^{-1}\ cat\ h^{-1}$ (1462.75 $\mu mol\ h^{-1}$ with FE of 98.01%), surpassing the performance of HG-CD-TPB, P-CN-Ph, and P-CN-TPB under the test current (Fig. 6c–d). During the H_2O_2 accumulation test, when operated at a current density of 80 $mA\ cm^{-2}$ for one hour, H_2O_2 was produced with stable electrode potential (Fig. S55). The Fenton reaction is a well-established method for pollutant treatment, wherein the reaction between Fe^{2+} and H_2O_2 generates hydroxyl radicals that can effectively react with pollutants⁴⁴. Leveraging the great $2e^-$ ORR electrocatalytic activity of the central phenyl group-containing HG-CD-Ph, we further used the generated H_2O_2 to degrade organic dyes (malachite green, rhodamine B, and methylene blue) (the detailed experiment was provided in Supplementary Information). The optical image clearly illustrates the rapid fading of malachite green, rhodamine B, and methylene blue from colored to colorless within a few minutes (Fig. 6e–f and S56). This study further supports the

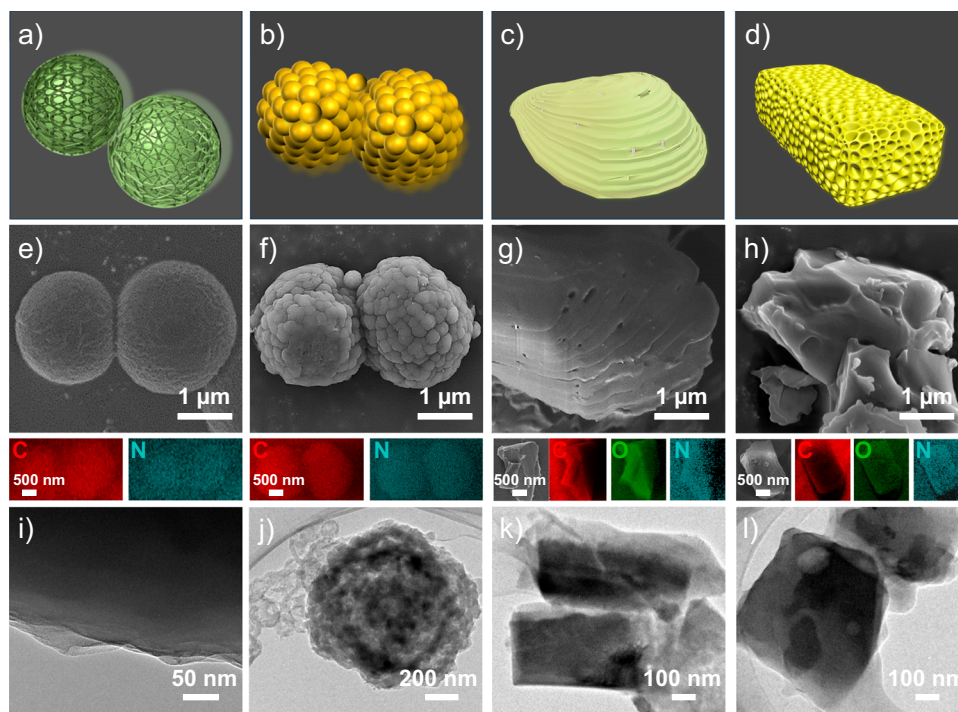


Fig. 4 | Microscopical characterization of the catalysts. **a–d** Modeling simulation images of P-CN-TPB, P-CN-Ph, HG-CD-TPB, and HG-CD-Ph. **e–h** SEM images, and EDS maps of P-CN-TPB, P-CN-Ph, HG-CD-TPB, and HG-CD-Ph. **i–l** Low-magnification TEM image of P-CN-TPB, P-CN-Ph, HG-CD-TPB, and HG-CD-Ph.

potential of HG-CD-Ph as an electrocatalyst for efficient H_2O_2 production by providing additional evidence with experiments on organic dye degradation. The results of these studies consistently indicate that HG-CD-Ph exhibits superior activity in the production of H_2O_2 (Fig. 6g).

Theoretical calculations

To gain further insights into the distinct performance of P-CN-TPB, P-CN-Ph, HG-CD-TPB, and HG-CD-Ph in 2e^- ORR, DFT calculations were carried out for these polymer models^{45–47}. All structures along the potential energy surfaces were optimized without any constraints (details about molecular configurations can be found in the Supplementary Data 1). In the calculation, the nomenclature of P-CN-TPB, P-CN-Ph, HG-CD-TPB, and HG-CD-Ph for these model molecules was maintained (Fig. 7a). In addition, possible active sites were selected to determine the overpotentials for H_2O_2 production (Figs. S57–60 and Tables S2–5). We presented vital geometrical parameters and the Mulliken charges on main atoms at stationary points along the reaction pathway of catalyzing 2e^- ORR in Fig. 7b^{48,49}. The shortened C–O bond produces a stronger charge transfer between HG-CD-Ph and O_2 . Figure 7c illustrates the partitioned density of states (PDOS) for total (purple lines), C atoms (green lines), N atoms (orange lines), and O atoms (pink lines) on P-CN-TPB, P-CN-Ph, HG-CD-TPB, and HG-CD-Ph. It could be found that the contribution of C is more significant in dynamic-bond-based supermolecule HG-CD-TPB and HG-CD-Ph than in covalent-bond-based polymers P-CN-TPB and P-CN-Ph, indicating that the introduction of host-guest interactions strengthens the electronic density of local C atoms. This enhancement may facilitate the interaction between the C and O_2 moieties during the reaction⁵⁰.

To gain a comprehensive understanding of the catalytic performance of dynamic-bond-based HG-CD-Ph and covalent-bond-based P-CN-Ph, the actual catalytically active centers were investigated by combining the in situ attenuated total reflectance Fourier transform infrared (ATR-FTIR) spectroscopic characterization and DFT calculations. Two theoretical transmission models (Fig. 8a and S61) were constructed to elucidate the potential transmission locations of the OOH^* intermediate. ATR-FTIR spectroscopic tests were conducted to

detect the crucially adsorbed OOH^* on HG-CD-Ph and P-CN-Ph during the electrolytic H_2O_2 synthesis. A weak transmission band at about 1210 cm^{-1} appears at a potential of 0.7 V vs RHE, which is gradually enhanced by decreasing the potential (Fig. 8b). These transmission bands on HG-CD-Ph can be assigned to O–O stretching vibration of OOH^* . Additionally, the bands at 976 cm^{-1} that increase with negatively shifted potential can be reasonably assigned to the O–H stretching mode of OOH^* . The spectral band assigned to adsorbed hydroperoxides (usually at 1386 cm^{-1}) is relatively poorer, as the generated H_2O_2 is immediately converted into HO_2^- products in alkaline environments^{51–53}. In comparison with theoretical infrared analysis, the measured peaks observed at 1030 cm^{-1} of P-CN-Ph exclusively correspond to the O–O stretching vibration (Fig. S62). The abundant OOH^* tensile vibration signals in HG-CD-Ph confirm that dynamic cross-linked host-guest-based supramolecules effectively regulate adsorption sites and facilitate the adsorption/desorption process of O_2 and its intermediates. Detecting potential-dependent transmitted hydroperoxyl bands provides evidence for the OOH^* mediated two-electron ORR pathway on both HG-CD-Ph and P-CN-Ph catalysts. Additional DFT calculations were further performed on the model compounds to ensure the catalytic active site of the as-prepared materials. The electron localization function (ELF) reveals that HG-CD-TPB and HG-CD-Ph enhanced localization around the $-\text{C}=\text{N}$ (N) atoms region (Fig. 8c, Left), conducting the ORR catalytic reaction^{54,55}. Electrophilic sites were further predicted by Fukui function to identify active sites. Notably, the isosurface maps progressively increase from P-CN-TPB, P-CN-Ph, and HG-CD-TPB to HG-CD-Ph. The highest distribution of isosurface map in HG-CD-Ph will favorably contribute to the adsorption of electrophilic oxygen intermediates (Fig. 8c, Right)^{56,57}. Thus, several sites with significant isosurfaces in the Fukui function were further selected as potential catalytic active sites for theoretical calculations (Figs. S63–64). The overpotential associated with the C atom located on the adamantane moiety (site-1) of the central phenyl group-containing HG-CD-Ph (0.07 eV) was lower than that of P-CN-Ph (0.5 eV) (Fig. 8d). Notably, this site exhibits the lowest free energy within the entire molecular system, thereby indicating its potential as a

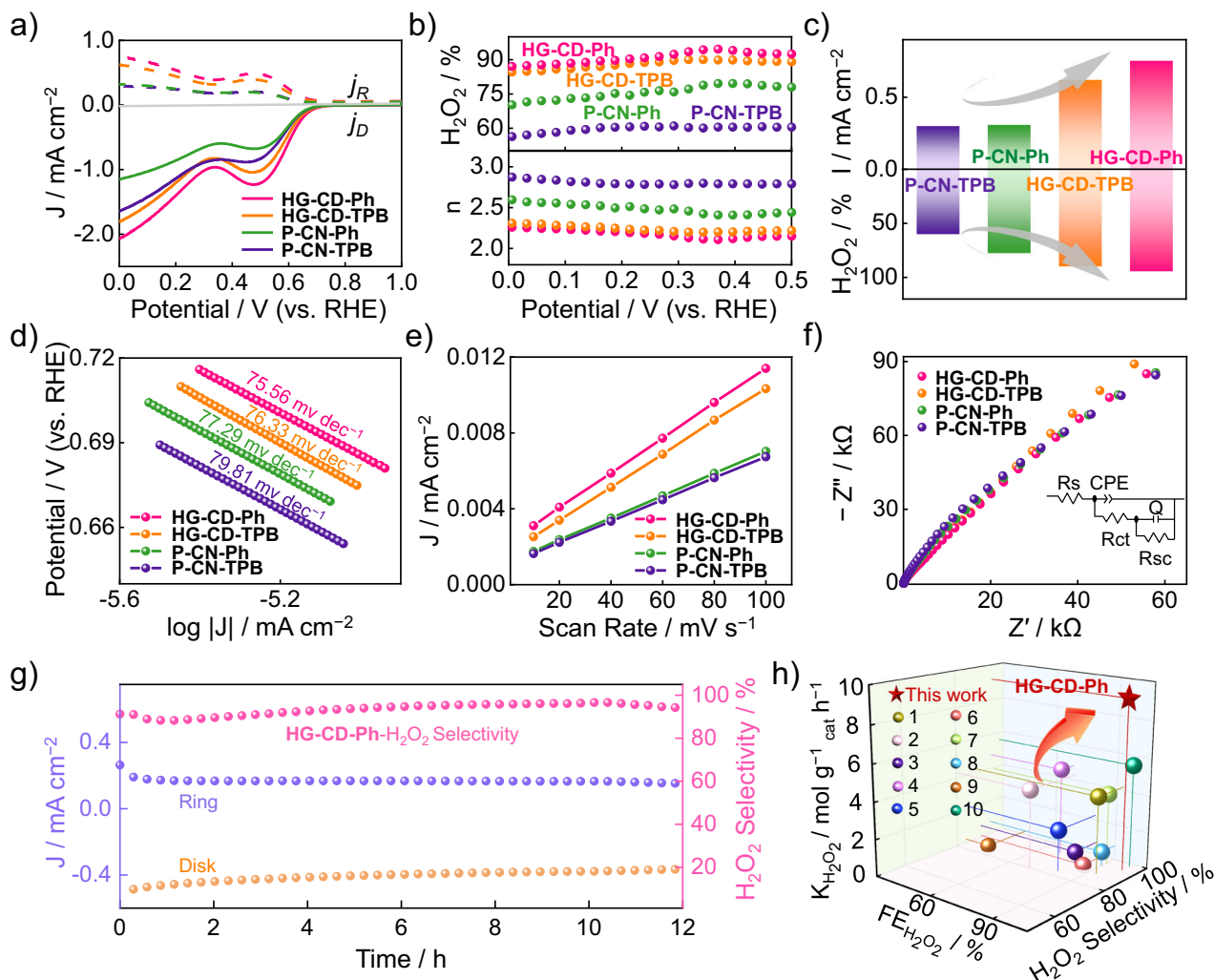


Fig. 5 | Electrochemical performance of the catalysts in rotating ring-disk electrode (RRDE). **a** LSV-RRDE without iR compensation. **b** The corresponding H_2O_2 selectivity profiles and the electron-transfer number in O_2 -saturated 0.1 M KOH electrolyte. **c** The 2e^- ORR comparison. **d** The corresponding Tafel plots. **e** C_{dl} values. **f** The EIS spectra of HG-CD-Ph, HG-CD-TPB, P-CN-Ph, and P-CN-TPB.

g Stability tests of HG-CD-Ph at a potential of 0.4 V vs RHE in O_2 -saturated 0.1 M KOH (test conditions: electrode area = 0.126 cm^2 , resistance in RRDE test system = $16.8 \pm 0.2 \Omega$). **h** The H_2O_2 selectivity, $K_{\text{H}_2\text{O}_2}$, and $\text{FE}_{\text{H}_2\text{O}_2}$ distributions of reported covalently bonded catalysts and metal-free organic supermolecule catalyst HG-CD-Ph (this work).

catalytically active site. To further explore the impact of connected bonds on activity and selectivity, the electron transfer from HG-CD-Ph to O_2 was examined. Figure 8e shows the highest occupied molecular orbital (HOMO) diagram of various polymers. The HOMO energy of HG-CD-Ph is -4.88 eV , closely resembling the LUMO energy of oxygen, resulting in more effortless electron transfer from HG-CD-Ph to oxygen⁵⁸. Therefore, the easier oxygen adsorption during the ORR process elucidates the heightened catalytic activity of HG-CD-Ph.

The reported studies have demonstrated that the ORR activity and selectivity can be attributed to the binding free energy of the reaction intermediate and the ORHP process⁵⁹. Consequently, the catalytic activity can be determined by the corresponding energy level of the crucial intermediate (OOH^*). The binding energy of OOH^* (ΔG_{OOH^*}) was employed as a descriptor and an activity volcano to estimate the activities of different connected bonds. The maximum U_L (zero overpotential at the top of the volcano) is determined to be 0.70 V. The calculated U_L as a function of ΔG_{OOH^*} for the ORHP process of these catalysts is shown in Fig. 8f. The structures positioned on the right side of the volcano present the weak binding energy of OOH^* , and on the left side, they strongly bind OOH^* , while the middle represents the theoretical optimal ΔG_{OOH^*} ^{60,61}. As a result, variations in the binding

strength of OOH^* in dynamic-crosslinked supramolecular polymers and covalent-linked polymers lead to diverse ORHP activities. The sites-1 on HG-CD-Ph is closer to the top of the volcano map, demonstrating the host-guest decoration is beneficial to ORHP for more moderate binding of OOH^* .

Discussion

In summary, we have successfully showcased a supramolecular host-guest approach that effectively modulates the electronic states for organic polymer electrocatalysts in 2e^- ORR. The dynamically tunable molecular network significantly enhances charge transfer within these structural frameworks, optimizes the electronic structure of active sites, and thereby influences the intrinsic activity of HG-CD-based molecules. Notably, the central phenyl group-containing HG-CD-Ph shows the highest H_2O_2 production rate of $9.14 \text{ mol g}^{-1} \text{ cat h}^{-1}$ and demonstrates a Faraday efficiency of 98.01% in alkaline electrolytes. Theoretical calculation results further revealed that the introduction of dynamic bonds can modulate the binding energy of OOH^* intermediate and optimize the local electron accumulation, precisely proving that the host-guest dynamic bonds endow C atoms of adamantane (site-1) adjacent to $-\text{C}=\text{N}$ (N) group as active sites. Overall,

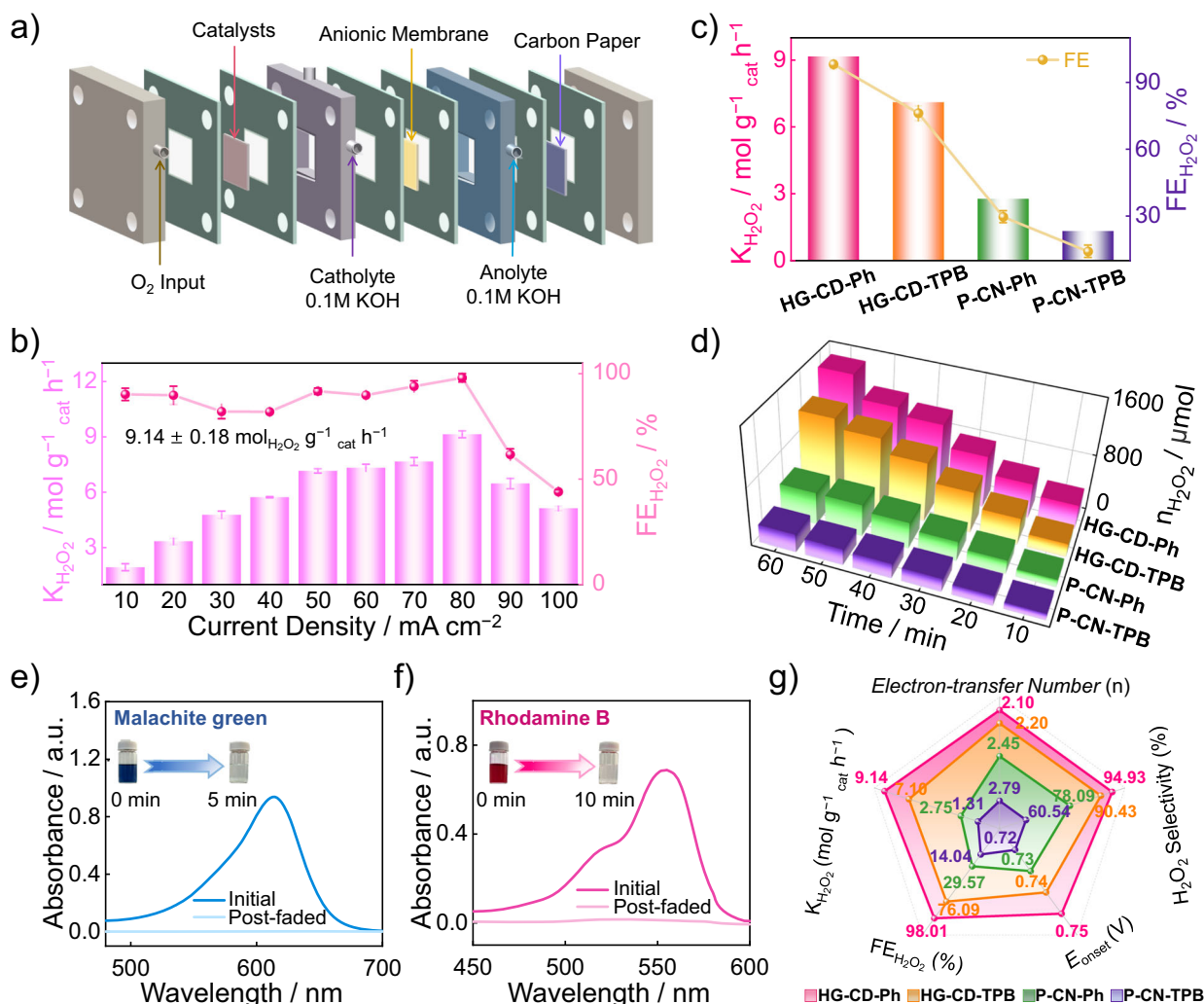


Fig. 6 | Performance of the catalysts in producing H_2O_2 within flow cells and application in dye degradation. **a** Schematic diagram showing the configuration with samples and carbon as cathodic and anodic catalysts. **b** $K_{H_2O_2}$ and $FE_{H_2O_2}$ of HG-CD-Ph of the flow cell operated under different current densities. **c** H_2O_2 production rate ($K_{H_2O_2}$) and corresponding faradaic efficiency ($FE_{H_2O_2}$). **d** H_2O_2 yield of HG-CD-Ph, HG-CD-TPB, P-CN-Ph, and P-CN-TPB tested under $80\ mA\ cm^{-2}$ (test conditions: resistance in flow cell test system = $8.6 \pm 0.1\ \Omega$). **e** Digital images for the decolorization of organic dyes (Malachite green). **f** Digital images for the decolorization of organic dyes (Rhodamine B). **g** The illustration of the relationship between activity and structure. (each experiment was independently tested three

times; sample size $n = 3$; mean \pm standard deviation (mean \pm SD) was analyzed using Origin software; SD reflects the degree of dispersion among individual samples; a small SD means that the value of the test is close to the average; the P -value indicates significant differences: HG-CD-Ph to HG-CD-TPB: $P < 0.0001$; HG-CD-TPB to P-CN-Ph: $P < 0.0001$; P-CN-Ph to P-CN-TPB: $P < 0.0001$; the statistical test was two-sided testing, the α -value was 0.05 and related P -values were analyzed by a two-side t-test of Student in GraphPad Prism software; P -values less than 0.0001 indicate that the differences between HG-CD-Ph to HG-CD-TPB, HG-CD-TPB to P-CN-Ph and P-CN-Ph to P-CN-TPB is particularly significant).

this work provides a promising approach to clarify the relationship between the catalytic capability of H_2O_2 production of supramolecular polymers and related dynamic bonds, which could expand the utilization of such host-guest catalysts in diverse electrocatalytic applications.

Methods

Chemicals and materials

All materials purchased from Aladdin, commercially available solvents, and reagents were used without further purification unless stated otherwise.

Synthesis of P-CN-TPB

4,4'-Biphenyldiamine (22.1 mg, 0.12 mmol) and 1,3,5-Benzene-tricarboxaldehyde (13.0 mg, 0.08 mmol) were weighed into a 10 mL Schlenk storage tube, dissolved in a mixed solvent (3 mL, 1,4-dioxane: mesitylene = 1: 1) and sonicated for 10 min. After that, aqueous HOAc

(0.3 mL, 6 mol/L) was added to the mixture. Finally, each tube was sealed off, heated at $120\ ^\circ C$ in an oven, and left undisturbed for 72 h. After cooling to room temperature, the tube was opened, and the yellow precipitates were filtered and washed three times with 1,4-dioxane, THF, and acetone, respectively. The solid was dried under vacuum at $120\ ^\circ C$ overnight to afford a yellow powder of 30.1 mg (86 % yield).

Synthesis of P-CN-Ph

4,4'-Biphenyldiamine (22.1 mg, 0.12 mmol) and 1,3,5-Tris-(p-formylphenyl) benzene (31.2 mg, 0.08 mmol) were weighed into a 10 mL Schlenk storage tube, dissolved in a mixed solvent (3 mL, 1,4-dioxane: mesitylene = 1: 1) and sonicated for 10 min. After that, aqueous HOAc (0.3 mL, 6 mol/L) was added to the mixture. Finally, each tube was sealed off, heated at $120\ ^\circ C$ in an oven, and left undisturbed for 72 h. After cooling to room temperature, the tube was opened, and the yellow precipitates were filtered and washed three times with 1,4-

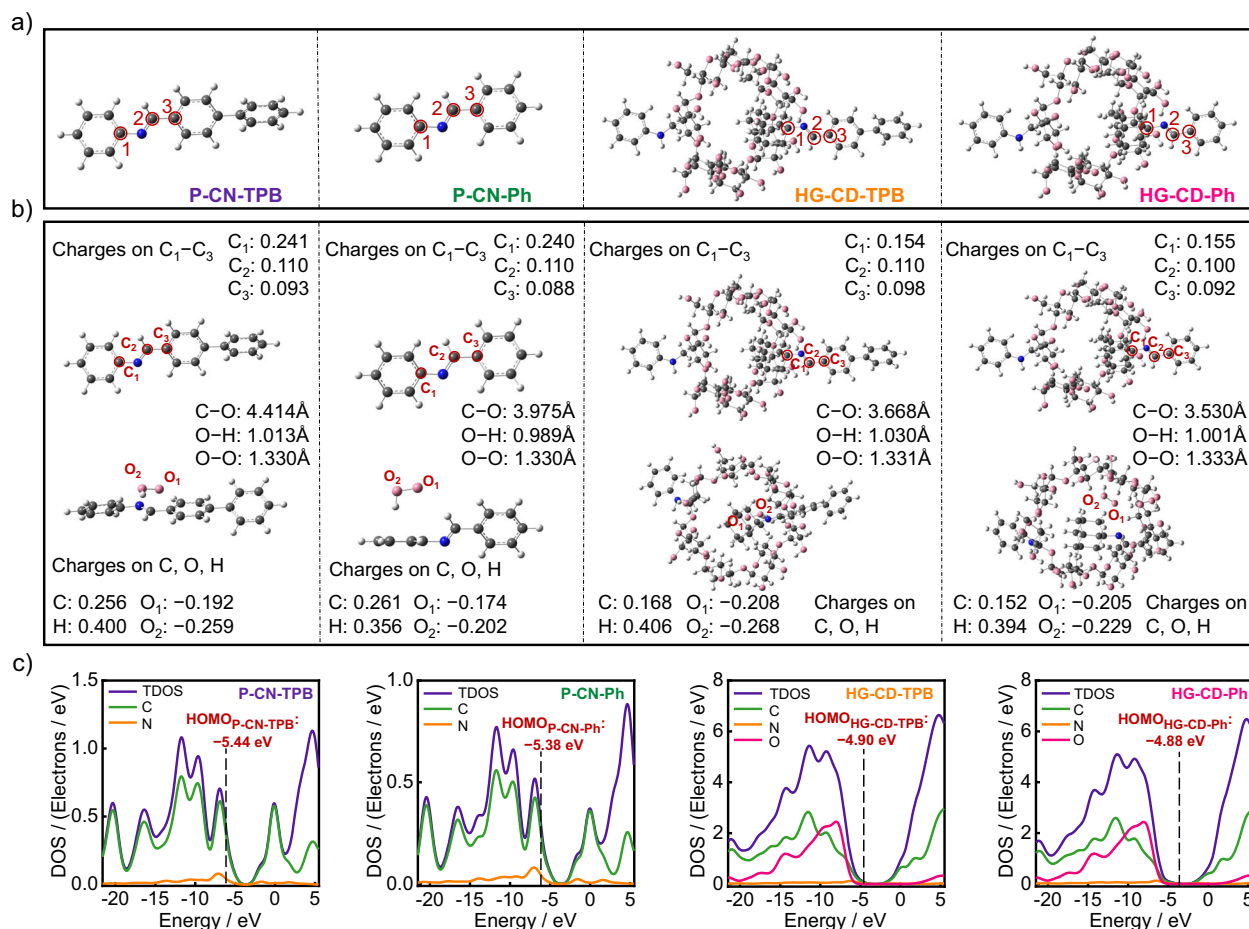


Fig. 7 | Theoretical calculation of the catalysts. **a** Optimized structures and active sites. **b** The main geometrical parameters and the Mulliken charges on main atoms of P-CN-TPB, P-CN-Ph, HG-CD-TPB, and HG-CD-Ph. Blue, gray, pink, and white spheres represent the N, C, O, and H atoms, respectively. **c** The total density of

states (TDOSs, purple lines), the partial density of states (PDOSs) of C (green lines), N (orange lines), and O (pink lines) for P-CN-TPB, P-CN-Ph, HG-CD-TPB, and HG-CD-Ph.

dioxane, THF, and acetone, respectively. The solid was dried under vacuum at 120 °C overnight to afford a yellow powder of 42.3 mg (79% yield).

Synthesis of BD-CD

4,4'-Biphenyldiamine (9.2 mg, 0.05 mmol) and mono[6-O-(p-toluenesulfonyl)]-β-CD (141.8 mg, 0.11 mmol) were dissolved in anhydrous DMF (40 mL), and the reaction mixture was stirred at 90 °C under nitrogen atmosphere for 24 h, followed by evaporation under reduced pressure to dryness. The residue was dissolved in a small amount of water, and the resultant solution was poured into acetone with vigorous stirring to obtain a brown-yellow precipitate. The crude product was collected by filtration and chromatographed on a SephadexG-25 column with water as eluent to give the pure, faint yellow solid with a 40% yield. (49.5 mg, 0.02 mmol). ¹H NMR (600 MHz, DMSO-*d*₆): δ 7.43 (m, 4H), 7.07 (m, 4H), 5.67 (m, 30H), 4.78 (s, 14H), 4.43 (s, 12H), 6.73 (m, 84H), 2.54 (s, 4H).

Synthesis of TPB-AD

Amantadine (36.3 mg, 0.24 mmol) and 1,3,5-Benzenetricarboxaldehyde (13.0 mg, 0.08 mmol) were dissolved in degassed toluene (10 mL), and the mixture was stirred at 120 °C for 24 h. After cooling to room temperature, the solution was diluted with methylene dichloride (30 mL) and water, and the organic phase was dried over anhydrous Na₂SO₄. The solvent was removed at reduced pressure to give a white solid with a 75% yield. (47.4 mg, 0.06 mmol). ¹H NMR (400 MHz,

Chloroform-*d*): δ 8.35 (s, 1H), 7.87 (m, 2H), 7.82 (s, 1H), 7.74 (m, 2H), 2.19 (s, 3H), 1.85 (s, 6H), 1.75 (m, 6H).

Synthesis of Ph-AD

Amantadine (36.3 mg, 0.24 mmol) and 1,3,5-Tris-(p-formylphenyl) benzene (31.2 mg, 0.08 mmol) were dissolved in degassed toluene (10 mL), and the mixture was stirred at 120 °C for 24 h. After cooling to room temperature, the solution was diluted with methylene dichloride (30 mL) and water, and the organic phase was dried over anhydrous Na₂SO₄. The solvent was removed at reduced pressure to give a white solid with an 87% yield. (39.3 mg, 0.07 mmol). ¹H NMR (400 MHz, Chloroform-*d*): δ 8.38 (s, 1H), 8.15 (s, 1H), 2.17 (s, 3H), 1.81 (s, 6H), 1.73 (m, 6H).

Synthesis of HG-CD-TPB

BD-CD and TPB-AD (CD: AD, 1: 1 stoichiometry) were separately dissolved in deionized water and THF, blended, and vigorously stirred for 24 h to form the inclusion complex, followed by the removal of the solvent under vacuum at 80 °C.

Synthesis of HG-CD-Ph

BD-CD and Ph-AD (CD: AD, 1: 1 stoichiometry) were separately dissolved in deionized water and THF, blended, and vigorously stirred for 24 h to form the inclusion complex, followed by removal of the solvent under vacuum at 80 °C.

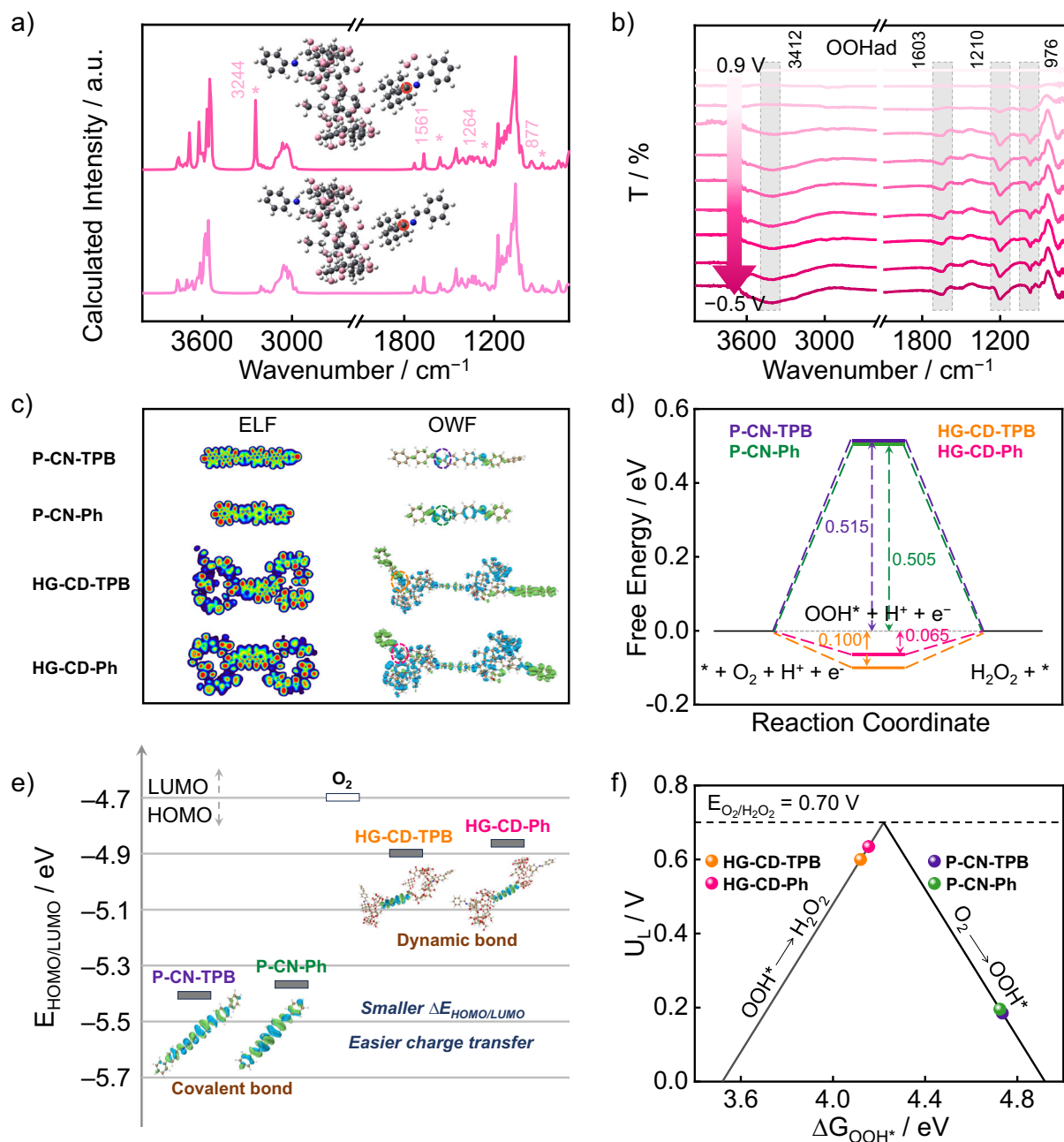


Fig. 8 | Theoretical and in situ detection of $^*\text{OOH}$ species and DFT calculations of the $2e^-$ ORR pathway on the catalysts. a Theoretical FT-IR spectra of the HG-CD-Ph model before (light pink line) and after (dark pink line) the adsorption of $^*\text{OOH}$ intermediates. Blue, gray, pink, and white spheres represent the N, C, O, and H atoms, respectively. **b** In situ electrochemical FT-IR spectra of HG-CD-Ph in O_2 -saturated 0.1 M KOH solution (pH = 13) ranging from -0.5 to 0.9 V versus RHE at an interval of 200 mV. The HOMO level of P-CN-TPB, P-CN-Ph, HG-CD-TPB, and HG-CD-Ph and O_2 . **c** Electron localization function (ELF, Left) and Orbit weight Fukui

function (OWF, Right, Blue, and green represent the positive and negative parts, respectively). **d** Free energy for ORHP of P-CN-TPB, P-CN-Ph, HG-CD-TPB, and HG-CD-Ph (at site-1). **e** The HOMO level of P-CN-TPB, P-CN-Ph, HG-CD-TPB, HG-CD-Ph, and O_2 . Blue, brown, red, and white spheres represent the N, C, O, and H atoms, respectively. **f** The calculated ORR activity volcano plot for $2e^-$ pathway to H_2O_2 of P-CN-TPB, P-CN-Ph, HG-CD-TPB, and HG-CD-Ph, equilibrium potential of $\text{O}_2/\text{H}_2\text{O}_2$ is shown as a black dashed line.

Material characterizations

The morphologies and structures of the samples were characterized by using field emission scanning electron microscopy (SEM) (JSM-7001F, JEOL, Tokyo, Japan) with an energy dispersive X-ray spectrometer (EDS) and the transmission electron microscopy (TEM) (JEM-1011; JEOL Co., Japan) operated at an accelerating voltage of 100 kV. Fourier transform infrared (FT-IR) data were performed on a Nicolet iS50 FTIR spectrometer (Thermo Fisher Scientific Co). Thermogravimetric analysis (TGA) was recorded on a SHIMADZU DTG-60 thermal

analyzer under N_2 . The operational range of the instrument was from 30 $^{\circ}\text{C}$ to 800 $^{\circ}\text{C}$ at a heating rate of 10 $^{\circ}\text{C min}^{-1}$ with an N_2 flow rate of 30 mL min^{-1} . The molecular packing was investigated by powder X-ray diffraction (PXRD). PXRD data were collected on a PANalytical B.V. Empyrean powder diffractometer using a $\text{Cu K}\alpha$ source ($\lambda = 1.5418 \text{ \AA}$) over the range of $2\theta = 2-40^{\circ}$ with a step size of 0.02° and 2 s per step. The contact angle is measured by the Attention Optical Contact Angle measuring instrument theta (Sweden baioulin Technology Co., Ltd). Ultraviolet-visible diffuse reflectance spectroscopy (UV-vis DRS) was

measured with a Shimadzu UV-3600 spectrometer. Current (I)-voltage (V) curves were performed on a CHI660a electrochemical workstation. ^1H NMR spectra were measured with a Bruker AV-600 spectrometer in Chloroform-*d* or DMSO-*d* at 25 °C. Chemical shift is reported in ppm using Chloroform-*d* (7.26 ppm) or DMSO-*d* (2.50 ppm) for ^1H NMR as an internal standard. 2D-Nosey spectra were measured with a Bruker AV-600 spectrometer in DMSO-*d* at 30 °C. Solid-state ^{13}C cross polarization-magic angle spinning nuclear magnetic resonance (^{13}C CP-MAS NMR) with Bruker AV-400. A gravimetric vapor adsorption analyzer performed the water vapor adsorption measurement (Micromeritics ASAP-2460). X-ray photoelectron spectroscopy (XPS) was conducted on an XPS instrument (Axis Supra). To estimate pore size distributions, nonlocal density functional theory (NLDFT) was applied to analyze the N_2 isotherm based on the model of $\text{N}_2@77\text{ K}$ on carbon with slit pores and the method of non-negative regularization. ICP-OES (Avio™ 200) was used to analyze metal contaminants.

Electrochemical tests in RRDE

The electrochemical tests were conducted on an RRDE on a CHI 760E workstation, coupled to an RRDE-3A (ALS Co, Ltd.) rotator: a glassy carbon disc electrode ($\varnothing = 4.0\text{ mm}$), a Pt ring electrode (\varnothing inner = 5.0 mm, \varnothing outer = 7.0 mm), a Pt wire was used as counter electrode and Ag/AgCl as reference electrode. Each catalyst (1.5 mg) was dispersed into 150 μL solution composed of 13: 13: 4 = ethanol: H_2O : Nafion (5 wt%) solution, and then the uniform catalyst ink was placed in an ultrasonic bath. 6 μL ink was loaded onto the RRDE electrode and dried at temperature. The calibration of Ag/AgCl electrodes was carried out with a three-electrode system in an H_2 -saturated 0.1 M KOH electrolyte (working electrode: Pt mesh, counter electrode: Pt wire, reference electrode: Ag/AgCl electrode). Linear sweep voltammetry (LSV) curves were performed at an electrode rotation rate of 1600 rpm and a potential sweep rate of 10 mV s^{-1} , with a ring potential held at +0.5 V vs Ag/AgCl (or +1.46 V vs. RHE). All potential scales were converted to RHE using: $E_{\text{RHE}} = E_{\text{Ag/AgCl}} + 0.059 \cdot \text{pH} + 0.1976$. The pH value of 0.1 M KOH electrolyte ($\text{pH} = 12.98 \pm 0.12$) was determined by a Mettler Toledo pH controller (Zurich, Switzerland) calibrated with pH buffer solutions ($\text{pH} = 6.86$). The electrochemical tests were performed without iR compensation. The H_2O_2 selectivity and electron transfer number were calculated using the following equations based on the LSV curves. A potential of 1.46 V (vs. RHE) was applied to the ring of the working electrode.

$$\text{H}_2\text{O}_2(\%) = 2 * (I_{\text{R}}/N)/(I_{\text{D}} + I_{\text{R}}/N) * 100\% \quad (1)$$

$$n = 4 * I_{\text{D}}/(I_{\text{D}} + I_{\text{R}}/N) \quad (2)$$

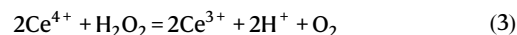
Where I_{R} is the ring current, I_{D} is the disk current, and N is the collection efficiency (0.47 after calibration).

LSV was performed in N_2 -saturated and O_2 -saturated 0.1 M KOH at a scan rate of 10 mV s^{-1} under various electrode rotation rates (400, 625, 900, 1225, 1600, 2025, and 2500 rpm, respectively). The internal resistance of the cell was evaluated by electrochemical impedance spectroscopy (EIS) from 0.1 to 10^6 Hz with an amplitude of 0.04 V. A long-term stability test was conducted by measuring the current changes of the catalyst at a fixed potential of 0.4 V (vs. RHE) at a rotation speed of 1600 rpm in an O_2 -saturated electrolyte using a CHI 760 E electrochemical workstation.

Electrochemical tests in flow cell

The H_2O_2 production process was performed in a self-assembled flow cell with a three-electrode system. A carbon paper with a microporous layer (area: 4 cm^2) was used as the working electrode. An Ag/AgCl and a carbon rod were applied as the reference and counter electrode, respectively. Pure O_2 was purged through the diffusion channel at a

flow rate of 100 mL min^{-1} , directed towards the rear of the gas-diffusion layer during the experimental procedure. For the chronopotentiometry test, various constant currents were applied by a CHI 760E electrochemistry station (CH Instrument) for 1 h, and for the accumulation test, 80 mA was employed for 1 h. The H_2O_2 concentrations were quantified by the conventional cerium sulfate $\text{Ce}(\text{SO}_4)_2$ titration method based on the theory that the yellow solution of Ce^{4+} would be reduced to a colorless Ce^{3+} solution by H_2O_2 based on the following equation. Thus, the consumed concentration of Ce^{4+} can be photometrically measured at the wavelength of 319 nm by UV-vis spectroscopy.



The 0.5 mmol L^{-1} Ce^{4+} standard solutions were obtained by dissolving 8.3 mg of $\text{Ce}(\text{SO}_4)_2$ in 50 mL of 0.5 mol L^{-1} H_2SO_4 . The sample solution was mixed with the standard Ce^{4+} solution by a volume ratio of 4: 30 to quantify the produced H_2O_2 . The Faraday efficiency (FE) and yield rate (YR) for H_2O_2 generation were calculated as follows:

$$C_{\text{H}_2\text{O}_2}(\text{mmol}) = [V_{\text{Ce}^{4+}} * C_{\text{before Ce}^{4+}} + -(V_{\text{Ce}^{4+}} + V_{\text{removed electrolyte}}) * C_{\text{after Ce}^{4+}}] * (V_{\text{electrolyte}}/V_{\text{removed electrolyte}})/2 \quad (4)$$

$$\text{YR}_{\text{H}_2\text{O}_2}(\text{mol g}^{-1} \text{ h}^{-1}) = C_{\text{H}_2\text{O}_2} / [Lg]/t/1000 \quad (5)$$

$$\text{FE}_{\text{H}_2\text{O}_2}(\%) = 2 * C_{\text{H}_2\text{O}_2} * F/(It) * 100\% \quad (6)$$

Where $C_{\text{H}_2\text{O}_2}$ is the molarity of generated H_2O_2 , $C_{\text{before Ce}^{4+}}$ is the molarity of the Ce^{4+} standard solution before the test, $C_{\text{after Ce}^{4+}}$ is the molarity of the Ce^{4+} solution after the test, $V_{\text{Ce}^{4+}}$ is the volume of the Ce^{4+} standard solution, $V_{\text{removed electrolyte}}$ is the volume of the removed electrolyte under test, $V_{\text{electrolyte}}$ is the total volume of the electrolyte under test, L is total mass of loaded catalysts on the RRDE electrode, F is the faraday constant, I and t are the operation current and time of the electrolysis test.

Dye decomposition test

For the decomposition of organic dye, 1 mL (1000 mg L^{-1}) FeSO_4 aqueous solution was added into 10 mL aqueous solution of malachite green or rhodamine B or methylene blue (60 mg L^{-1}), followed by 5 mL of the electrolyte from the cathodic tank after 1-hour accumulation test. After thoroughly mixing, transfer 3 mL into a glass bottle. Subsequently, photographs were captured based on the time sequence of 0 minutes and complete fading, while UV-vis adsorption spectra were scanned in the same chronological order.

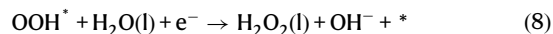
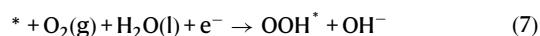
In situ ATR-FT-IR measurements

In situ attenuated total reflection Fourier transform infrared spectroscopy (ATR-FTIR) was performed on the Perkin Elmer spectrum 3 spectrometer. A thin layer of gold film is chemically deposited on the surface of the silicon crystal, and then 100 microliters of catalyst ink (10 mg L^{-1}) is dropped on the gold film, and the entire device acts as a working electrode. A platinum sheet was used as the counter electrode, and Ag/AgCl as the reference electrode. The electrolyte was 0.1 M KOH. Before the test, high-purity O_2 was introduced into the electrolyte for 30 minutes until O_2 was saturated in the electrolyte. Then, the i-t test was carried out in the range of -0.5 - 0.9 V vs. Ag/AgCl potential, and relevant ATR-FTIR spectra were collected.

Computational details

B3LYP hybrid density functional theory of Gaussian 09 was employed with a basis set of 6-31 G (d, p)⁶²⁻⁶⁶.

The overall ORR in an alkaline environment can be written as follows⁶⁷:



where $*$ and OOH^* denote an unoccupied active site and adsorbed OOH^* intermediate, respectively. Gibbs reaction free energy ΔG is defined as the difference between free energies of the initial and final states and is given by the expression:

$$\Delta G = \Delta E + \Delta \text{ZPE} - T\Delta S + \Delta G_{\text{U}} + \Delta G_{\text{pH}} \quad (9)$$

where ΔE is the reaction energy of reactant and product molecules adsorbed on the catalyst surface, obtained from DFT calculations; ΔZPE and ΔS are the changes in zero-point energies and entropy due to the reaction.

During the two-electron ORR process, the limiting step is determined by both OOH^* formation (Eq. (7)) and OOH^* removal (Eq. (8)) from the catalytic sites. The theoretical overpotential is demonstrated to be a function of the OOH^* binding energy, thus the limiting potential can be expressed as:

$$U_{\text{L1}} = -\Delta G_{\text{OOH}^*} + 4.92 \quad (10)$$

$$U_{\text{L2}} = \Delta G_{\text{OOH}^*} - 3.52 \quad (11)$$

Data availability

All data needed to evaluate the conclusions in the paper are provided in the Supplementary Information or Source Data file. Source data are provided with this paper.

References

- Chen, J. et al. Kinetically restrained oxygen reduction to hydrogen peroxide with nearly 100% selectivity. *Nat. Commun.* **13**, 2808 (2022).
- Cui, X. et al. Engineering organic polymers as emerging sustainable materials for powerful electrocatalysts. *Chem. Soc. Rev.* **53**, 1447–1494 (2024).
- Sun, Y. et al. A comparative perspective of electrochemical and photochemical approaches for catalytic H_2O_2 production. *Chem. Sov. Rev.* **49**, 6605–6631 (2020).
- Perry, S. C. et al. Electrochemical synthesis of hydrogen peroxide from water and oxygen. *Nat. Rev. Chem.* **3**, 442–458 (2019).
- Zhang, X. et al. Electrochemical oxygen reduction to hydrogen peroxide at practical rates in strong acidic media. *Nat. Commun.* **13**, 2880 (2022).
- Don, L.-Y. et al. Boundary-rich carbon-based electrocatalysts with manganese(II)-coordinated active environment for selective synthesis of hydrogen peroxide. *Angew. Chem., Int. Ed.* **63**, e20237660 (2024).
- Lu, Z. et al. High-efficiency oxygen reduction to hydrogen peroxide catalysed by oxidized carbon materials. *Nat. Catal.* **1**, 156–162 (2018).
- Li, Z. et al. Potent charge-trapping for boosted electrocatalytic oxygen reduction. *Adv. Energy Mater.* **13**, 2203963 (2023).
- Cui, P. et al. Carbon-based electrocatalysts for acidic oxygen reduction reaction. *Angew. Chem., Int. Ed.* **62**, e202218269 (2023).
- Guo, Y. et al. Steering sp-carbon content in graphdiynes for enhanced two-electron oxygen reduction to hydrogen peroxide. *Angew. Chem., Int. Ed.* **63**, e202401501 (2024).
- Zhou, X. et al. Constructing sulfur and oxygen supercoordinated main-group electrocatalysts for selective and cumulative H_2O_2 production. *Nat. Commun.* **15**, 193 (2024).
- Wu, H. et al. Topology control of covalent organic frameworks with interlaced unsaturated 2D and saturated 3D units for boosting electrocatalytic hydrogen peroxide production. *Angew. Chem., Int. Ed.* **63**, e202410719 (2024).
- Wu, Q. et al. Unveiling the dynamic active site of defective carbon-based electrocatalysts for hydrogen peroxide production. *Nat. Commun.* **14**, 6275 (2024).
- Lee, B.-H. et al. Supramolecular tuning of supported metal phthalocyanine catalysts for hydrogen peroxide electrosynthesis. *Nat. Catal.* **6**, 234–243 (2023).
- Amabilino, D. B. et al. Supramolecular materials. *Chem. Sov. Rev.* **46**, 2404–2420 (2017).
- Fu, H. et al. Supramolecular polymers form tactoids through liquid-liquid phase separation. *Nature* **626**, 1011–1018 (2024).
- Su, Y. et al. Hypercrosslinked polymer gels as a synthetic hybridization platform for designing versatile molecular separators. *J. Am. Chem. Soc.* **146**, 15479–15487 (2024).
- Ogoshi, T. et al. Applications of pillar[n]arene-based supramolecular assemblies. *Angew. Chem., Int. Ed.* **58**, 2197–2206 (2019).
- Yan, M. et al. Recent progress of supramolecular chemotherapy based on host-guest interactions. *Adv. Mater.* **36**, 2304249 (2024).
- Kasprzak, A. et al. Supramolecular chemistry of sumanene. *Angew. Chem., Int. Ed.* **63**, e202318437 (2024).
- Roy, N. et al. Supramolecular polymers: inherently dynamic materials. *Acc. Chem. Res.* **57**, 349–361 (2024).
- Alsbaiee, A. et al. Rapid removal of organic micropollutants from water by a porous β -cyclodextrin polymer. *Nature* **529**, 190–194 (2016).
- Ma, J. et al. Preparation of aromatic β -cyclodextrin nano/microcapsules and corresponding aromatic textiles: A review. *Carbohydr. Polym.* **308**, 120661 (2023).
- Gomez-Gonzalez, B. et al. Delving into the variability of supramolecular affinity: self-ion pairing as a central player in aqueous host-guest chemistry. *Angew. Chem., Int. Ed.* **63**, e202317553 (2024).
- Ma, R. et al. Linker mediated electronic-state manipulation of conjugated organic polymers enabling highly efficient oxygen reduction. *Angew. Chem. Int. Ed.* **63**, e202405594 (2024).
- Deng, M. et al. General design concept of high-performance single-atom-site catalysts for H_2O_2 electrosynthesis. *Adv. Mater.* **36**, 2314340 (2024).
- Liu, Y. et al. Electronic metal-support interactions boost $^*\text{OOH}$ intermediate generation in $\text{Cu}/\text{In}_2\text{Se}_3$ for electrochemical H_2O_2 production. *Angew. Chem., Int. Ed.* **63**, e202319470 (2024).
- Jin, J. et al. High-efficiency ternary polymer solar cells with a gradient-blended structure fabricated by sequential deposition. *ACS Appl. Mater. Interfaces* **16**, 15121–15132 (2024).
- Lu, T. et al. Multiwfn: a multifunctional wavefunction analyzer. *J. Comput. Chem.* **33**, 580–592 (2012).
- Zhang, J. et al. Efficient evaluation of electrostatic potential with computerized optimized code. *Phys. Chem. Chem. Phys.* **23**, 20323 (2021).
- You, Z. et al. Metal-free carbon-based covalent organic frameworks with heteroatom-free units boost efficient oxygen reduction. *Adv. Mater.* **35**, 2209129 (2023).

32. Wang, Q. et al. Positional thiophene isomerization: a geometric strategy for precisely regulating the electronic state of covalent organic frameworks to boost oxygen reduction. *Angew. Chem., Int. Ed.* **63**, e202320037 (2024).
33. Politzer, P. et al. Average local ionization energies as a route to intrinsic atomic electronegativities. *J. Chem. Theory Comput.* **7**, 377–384 (2011).
34. Politzer, P. et al. Average local ionization energy: a review. *J. Mol. Model.* **16**, 1731–1742 (2010).
35. Kandambeth, S. et al. Selective molecular sieving in self-standing porous covalent-organic-framework membranes. *Adv. Mater.* **29**, 1603945 (2017).
36. Guo, D. et al. Active sites of nitrogen-doped carbon materials for oxygen reduction reaction clarified using model catalysts. *Science* **351**, 361–365 (2016).
37. Yuan, Z. et al. The origin of superhydrophobicity for intrinsically hydrophilic metal oxides: A preferential O₂ adsorption dominated by oxygen vacancies. *Angew. Chem., Int. Ed.* **58**, 17406–17411 (2019).
38. Zhang, T. et al. Dynamic cross-linking of zwitterionic polymer binder based on host-guest interactions for Li-S batteries with enhanced safety and electrochemical performance. *Nano Energy* **114**, 108603 (2023).
39. Böhm, I. et al. Cyclodextrin and adamantane host-guest interactions of modified hyperbranched poly (ethylene imine) as mimetics for biological membranes. *Angew. Chem., Int. Ed.* **50**, 7896–7899 (2011).
40. Sugane, K. et al. Self-healing thermoset polyurethanes utilizing host-guest interaction of cyclodextrin and adamantane. *Polymer* **221**, 123629 (2021).
41. Sévery, L. et al. Immobilization of molecular catalysts on electrode surfaces using host-guest interactions. *Nat. Chem.* **13**, 523–529 (2021).
42. Roithmeyer, H. et al. Electrocatalytic ammonia oxidation with a tailored molecular catalyst heterogenized via surface host-guest complexation. *J. Am. Chem. Soc.* **146**, 430–436 (2024).
43. Yang, J. et al. A Full-spectrum porphyrin-fullerene d-a supramolecular photocatalyst with giant built-in electric field for efficient hydrogen production. *Adv. Mater.* **33**, 2101026 (2021).
44. Luo, Z. et al. High H₂O₂ selectivity and enhanced Fe²⁺ regeneration toward an effective electro-Fenton process based on a self-doped porous biochar cathode. *Appl. Catal. B-Environ.* **315**, 121523 (2022).
45. Ditchfield, R. et al. Self consistent molecular orbital methods. IX. an extended gaussian type basis for molecular orbital studies of organic molecules. *J. Chem. Phys.* **54**, 724–728 (1971).
46. Hehre, W. et al. Self-consistent molecular orbital methods. XII. further extensions of gaussian-type basis sets for use in molecular orbital studies of organic molecules. *J. Chem. Phys.* **56**, 2257–2261 (1972).
47. Martin, M. L. et al. On the integration accuracy in molecular density functional theory calculations using Gaussian basis sets. *Comput. Phys. Commun.* **133**, 189–201 (2001).
48. Machmer, P. et al. Charge transfer between nucleic acid bases and chloranil. *Nature* **206**, 618–619 (1965).
49. Khadka, D. B. et al. Defect passivation in methylammonium/bromine free inverted perovskite solar cells using charge-modulated molecular bonding. *Nat. Commun.* **15**, 882 (2024).
50. Liu, M. et al. Post-synthetic modification of covalent organic frameworks for CO₂ electroreduction. *Nat. Commun.* **14**, 3800 (2023).
51. Cao, P. et al. Metal single-site catalyst design for electrocatalytic production of hydrogen peroxide at industrial-relevant currents. *Nat. Commun.* **14**, 172 (2023).
52. Li, L. et al. Electrochemical generation of hydrogen peroxide from a zinc gallium oxide anode with dual active sites. *Nat. Commun.* **14**, 1890 (2023).
53. Fang, Y. et al. Boosting hydrogen peroxide electrosynthesis via modulating the interfacial hydrogen-bond environment. *Angew. Chem. Int. Ed.* **62**, e202304413 (2023).
54. Tian, L. U. et al. Meaning and functional form of the electron localization function. *Acta Phys.-Chim. Sin.* **27**, 2786–2792 (2011).
55. Reimann, M. et al. Rydberg electron stabilizes the charge localized state of the diamine cation. *Nat. Commun.* **15**, 293 (2024).
56. Ayers, P. W. et al. Variational principles for describing chemical reactions: the fukui function and chemical hardness revisited. *J. Am. Chem. Soc.* **122**, 2010–2018 (2000).
57. Yan, X. et al. An unsaturated bond strategy to regulate active centers of metal-free covalent organic frameworks for efficient oxygen reduction. *Angew. Chem., Int. Ed.* **61**, e202209583 (2022).
58. Finkelmeyer, S. J. et al. Tailoring the weight of surface and intralayer edge states to control lumo energies. *Adv. Mater.* **35**, 2305006 (2023).
59. Yan, X. et al. Tuning oxygen-containing groups of pyrene for high hydrogen peroxide production selectivity. *Appl. Catal. B-Environ.* **304**, 120908 (2022).
60. Kim, C. et al. Concurrent oxygen reduction and water oxidation at high ionic strength for scalable electrosynthesis of hydrogen peroxide. *Nat. Commun.* **14**, 5822 (2023).
61. Yan, M. et al. Sb₂S₃-templated synthesis of sulfur-doped Sb-N-C with hierarchical architecture and high metal loading for H₂O₂ electrosynthesis. *Nat. Commun.* **14**, 368 (2023).
62. Radom, L. et al. Molecular orbital theory of the electronic structure of organic compounds. VIII. Geometries, energies, and polarities of C3 hydrocarbons. *J. Am. Chem. Soc.* **93**, 5339–5342 (1971).
63. Hehre, W. J. et al. Self-consistent molecular-orbital methods. I. use of Gaussian expansions of Slater-Type atomic orbitals. *J. Chem. Phys.* **51**, 2657–2664 (1969).
64. Franci, M. M. et al. Self-consistent molecular orbital methods. XXIII. a polarization-type basis set for second-row elements. *J. Chem. Phys.* **77**, 3654–3665 (1982).
65. Jiao, Y. et al. Design of electrocatalysts for oxygen- and hydrogen-involving energy conversion reactions. *Chem. Soc. Rev.* **44**, 2060–2086 (2015).
66. Seh, Z. W. et al. Combining theory and experiment in electrocatalysis: insights into materials design. *Science* **355**, eaad4998 (2017).
67. Nørskov, J. K. et al. Origin of the overpotential for oxygen reduction at a fuel-cell cathode. *J. Phys. Chem. B* **108**, 17886–17892 (2004).

Acknowledgements

The authors are grateful for the financial support from the National Natural Science Foundation of China (Nos. 22375111 and 22075157 (X.J.L.)), the Taishan Scholars Program (No. tsqn201909090 (X.J.L.)), the Natural Science Foundation and Youth Innovation Team Project of Shandong Province, China (Nos. ZR2024JQ037, 2021KJ018 and ZR2021YQ08 (X.J.L.)), and the Qingdao New Energy Shandong Laboratory Open Project (QNESLOP202310 (X.J.L.)).

Author contributions

X.J.L. designed the experiments. H.N.C. prepared the samples and performed most of the electrocatalytic measurements. C.W. performed the theoretical calculations. H.W., L.L.L., Y.L.X., and C.H.Z. performed some material characterization. H.N.C. and X.J.L. wrote the manuscript with input from all authors. H.N.C. and C.W. contributed equally to this work. All authors discussed the obtained results.

Competing interests

The authors declare no competing interests.

Additional information

Supplementary information The online version contains supplementary material available at <https://doi.org/10.1038/s41467-024-53714-3>.

Correspondence and requests for materials should be addressed to Xiaojing Long.

Peer review information *Nature Communications* thanks the anonymous reviewers for their contribution to the peer review of this work. A peer review file is available.

Reprints and permissions information is available at <http://www.nature.com/reprints>

Publisher's note Springer Nature remains neutral with regard to jurisdictional claims in published maps and institutional affiliations.

Open Access This article is licensed under a Creative Commons Attribution-NonCommercial-NoDerivatives 4.0 International License, which permits any non-commercial use, sharing, distribution and reproduction in any medium or format, as long as you give appropriate credit to the original author(s) and the source, provide a link to the Creative Commons licence, and indicate if you modified the licensed material. You do not have permission under this licence to share adapted material derived from this article or parts of it. The images or other third party material in this article are included in the article's Creative Commons licence, unless indicated otherwise in a credit line to the material. If material is not included in the article's Creative Commons licence and your intended use is not permitted by statutory regulation or exceeds the permitted use, you will need to obtain permission directly from the copyright holder. To view a copy of this licence, visit <http://creativecommons.org/licenses/by-nc-nd/4.0/>.

© The Author(s) 2024